Korean J. Chem. Eng., 37(10), 1795-1802 (2020)
DOI: 10.1007/s11814-020-0559-5

pISSN: 0256-1115
eISSN: 1975-7220

Silicon and porous MWCNT composite as high capacity anode for lithium-ion batteries

Arunakumari Nulu, Venugopal Nulu, and Keun Yong Sohn†

Department of Nanoscience and Engineering, Center for Nano Manufacturing, Inje University,
197 Inje-ro, Gimhae, Gyeongnam-do 50834, Korea
(*Received 7 December 2019 • Revised 5 April 2020 • Accepted 27 April 2020*)

Abstract−A silicon/porous multi-walled carbon nanotubes composite was synthesized using a simple method. A mixture comprising silicon nanoparticles and multi-walled carbon nanotubes was prepared by a mini ball milling method followed by annealing at low temperature. The low-temperature annealing treatment allows the aggregation of silicon nanoparticles and propels them to adhere to the outer walls of carbon nanotubes without the formation of a SiO_x layer on Si nanoparticles. Mild oxidation occurring on the carbon tube walls provides additional surface defects. The obtained composite, which was studied as an anode for Li-ion batteries, exhibited excellent cyclability and superior rate capability compared with pristine silicon nanoparticles. The improved electrochemical performance of the composite can be attributed to the electrically conductive carbon tubes, easy access of the electrolyte ions into the porous nanotube walls, and mechanical support provided by the carbon matrix. As a result, the proposed composite can sustain high discharge capacities of 1,685 mAh g^{-1} at 1C rate after 80 cycles and 913 mAh g^{-1} at 5C rate after 100 cycles.

Keywords: Silicon, Porous Carbon Nano-tubes, Composite, Anode Material, Li-ion Batteries

INTRODUCTION

Rechargeable lithium-ion batteries (LIBs) are regarded as among the most promising secondary batteries available in the current portable electronics market owing to their high power, energy densities, and long cell life. The high energy efficiency and high power density of LIBs may increase their applications in long range electric vehicles, electric grid applications, and energy harvesting systems. For practical use in the new technology of energy storage systems, LIBs should be able to maintain long-term cycle stability with high specific capacity and coulombic efficiency. Moreover, with recent advances and further improvements, LIBs can support the development of future electric vehicles. It is well known that the anode and cathode materials employed in LIBs are detrimental to the overall performance of the LIBs. Several research studies have been conducted to develop new battery materials with low cost and high performance, which can further enhance the practical applications of LIBs [1-5]. The electrode materials with high specific capacity and good structural stability are required to exhibit high energy density and power density. Graphite, with a theoretical capacity of 372 mAh g^{-1}, is the most commonly used anode material for LIBs because of its long cycle life, availability, and low-cost production [6,7]. However, graphite also has certain drawbacks, such as its relatively low theoretical specific capacity. Hence, other anode materials have been investigated to meet high energy capacity requirements. Among them, Si has been studied extensively for its application as an anode material for LIBs due to its high theoretical specific capacity (4,200 mAh g^{-1}), which is nearly ten-times higher than that of the graphite at low working potential (~0.4 V vs. Li/Li^+) [8-11]. However, Si experiences significant volume changes (>300%) and pulverization during lithium insertion and extraction, resulting in rapid capacity loss. Moreover, the formation of an unstable solid electrolyte interface (SEI) has deterred its widespread application [12-14]. To address these limitations, comprehensive approaches have been developed to overcome the significant volume changes in the Si-based electrode and its low-electronic conductivity; these include the preparation of nanoscale silicon particles with carbon coating or fabrication of composites using a carbon matrix [15,16].

Owing to their high conductivity, high surface area, thermal stability, and high flexibility, carbon, and its related materials such as graphene, graphite, nanotubes, and carbon paste are excellent candidates for energy storage devices [17,18]. Due to the charge transfer limit, 2D and 3D scaffolds comprising hierarchically porous carbon materials and their composites are advantageous for LIBs, supercapacitors, and photovoltaics among other applications [19-23]. Some examples of these applications include the Cu-Ni Oxide@Graphene nanocomposite for high power and durable LIBs prepared by Louis Perreault et al. [18]. Pedico et al. reported an rGO aerogel decorated with copper and molybdenum sulfides on carbon fibers for high performing and wearable supercapacitors [24]. Liu et al. developed a MoO_2 nanoparticles/carbon textiles cathode for a high performance flexible Li-O_2 battery [25]. Luo et al. fabricated all-carbon electrode-endurable flexible perovskite solar cells [26]. Shih et al. developed carbon fiber penetrated sulfur crystals as a cathode material for lithium-sulfur batteries [27]. Bella et al. developed paper-based quasi-solid dye-sensitized solar cells with cellulose-based electrodes and electrolytes [28]. Zolin et al. devel-

†To whom correspondence should be addressed.
E-mail: ksohn@inje.ac.kr, ksohnlab@gmail.com

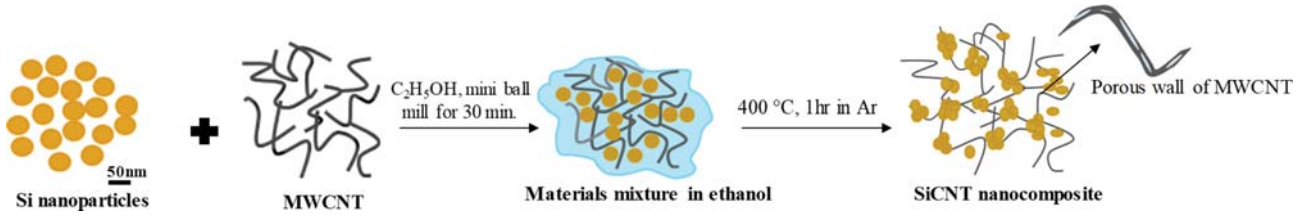

Fig. 1. Schematic illustration of the preparation method of the SiCNT nanocomposite.

oped a carbonized cellulose-based self-supporting electrode [29]. In a composite electrode, carbon provides both conductive support and mechanical stability, which could result in improved electrochemical performance of the Si-carbon composite electrode [30-33]. As mentioned above, the carbon and its related materials play an essential role in the development of novel types of electrode materials and improving the overall battery performance.

Multi-walled carbon nanotubes (MWCNTs) have received considerable attention as anode materials of LIBs owing to their abundant physical properties, such as high surface area, excellent electrical conductivity, thermal and mechanical properties, as well as their commercial availability [34-36]. Therefore, MWCNTs are regarded as suitable candidates for fabricating composites with silicon; this will ensure that the advantages of both Si and CNTs can be utilized to improve conductivity and cyclability while also precluding the disintegration of electrodes [37,38]. In previous works, Si/MWCNT composites were prepared by surface functionalization of Si particles followed by spray drying [39], CVD [38], acid etching of silicon particles and then making a composite with graphene and MWCNT [40], liquid injection CVD [41], and co-axial electrospinning [42]. All these composites worked effectively as anodes for Li-ion battery applications. However, these methods involve highly sophisticated equipment, multi-step processes, tiresome experimental parameters with extra demerits including reproducibility with gram-scale yields. In the case of silicon particles, the reported approaches discussed conventional high-temperature treatment in inert gas: it is used for the fabrication of Si-carbon composites; however, during the heat treatment process, the Si particle surface is oxidized, to some extent, to SiO_x, which reduces the overall specific capacity driven by the electrode. This is a common issue during high-temperature heat treatment [37-39]. Hence, a significant facile method, which utilizes low-temperature heat treatment with minimum laboratory facilities, has to be developed. Selecting a possible efficient carbon material that is capable of making a composite with an active material using low heat is another important task. To fulfill these requirements, MWCNTs have drawn our attention as a suitable carbon material to composite with Si nanoparticles.

In the present study, we proposed the fabrication of a composite composed of silicon nanoparticles attached to the porous walls of an MWCNT using a simple low-temperature annealing treatment. This Si/MWCNT network could relieve the addition of conductive carbon during electrode preparation. The composite exhibits superior electrochemical performance with greater specific capacity and a much more stable cycle retention compared to that of electrodes prepared from pure Si nanoparticles.

EXPERIMENTAL

1. Materials and Methods

Silicon nanocrystalline powder (Alfa Aesar, ≤50 nm), MWCNT (Hanwha Nanotech Corp. CM-100, diameter: 10 nm-14 nm), and ethanol solvent (Sigma-Aldrich, ≥99.5%) were purchased and used as received. The composite structures of the Si/porous MWCNT were prepared by mini milling followed by a low-temperature annealing method. The step-by-step fabrication process for the Si/MWCNT composite is shown in Fig. 1. First, silicon nanopowder and MWCNT were mixed in a 9 : 1 mass ratio. Then, a small amount of ethanol was added to the mixture. The mixture was brought into a zirconium bowl of the mini-mill and mixed well for approximately 30 min at a speed of 30 oscillations per second. The resulting slurry was taken into an alumina crucible and calcined at 400 °C for 1 h in a tube furnace under argon atmosphere. After heating, the furnace was cooled to room temperature. The obtained product was called SiCNT. The yield of the SiCNT was approximately 93.2% (0.932 g) of the total original weight of the materials. This loss of 6.8% in weight could be attributed to either the annealing process or to the occurrence of error during the collection of the sample from the crucible. For comparison, an electrode was prepared with Si nanoparticles and ketjen black as the carbon additive and was called SKB. The same experimental conditions followed for SiCNT were used to develop another composite to verify the reproducibility and was termed as R-SiCNT.

2. Chemical Analysis and Characterization Techniques

To visualize the crystal structure of the prepared composite material, X-ray diffraction (XRD) was used. In addition, the composite material was analyzed by Raman spectroscopy. For morphological characterization, scanning electron microscopy (SEM) and transmission electron microscopy (TEM) were used. Thermo-gravimetric analysis (TGA) was carried out from 25 °C to 800 °C in air.

3. Electrochemical Analysis

The electrochemical measurements were evaluated using 2032R-type coin cells. The working electrode was prepared by adding 80 wt% of the as-obtained SiCNT and 20 wt% of polyamide-imide (PAI) as a binder in 2-methyl N-pyrrolidone (NMP). No extra conductive carbon additive was added during the fabrication of the electrode. The SKB electrode was fabricated by adding 70 wt% of bare Si nanoparticles to 10 wt% of ketjen black conductive additive, and 20 wt% of PAI as a binder. The components were mixed well by the mini-mill for 30 min. The resulting slurry was uniformly coated on a copper foil using a doctor blade with 15 μm thickness. The electrode was dried at 80 °C for 2 h to evaporate the NMP. To activate the PAI binder, the oven-dried electrode was kept in a vac-

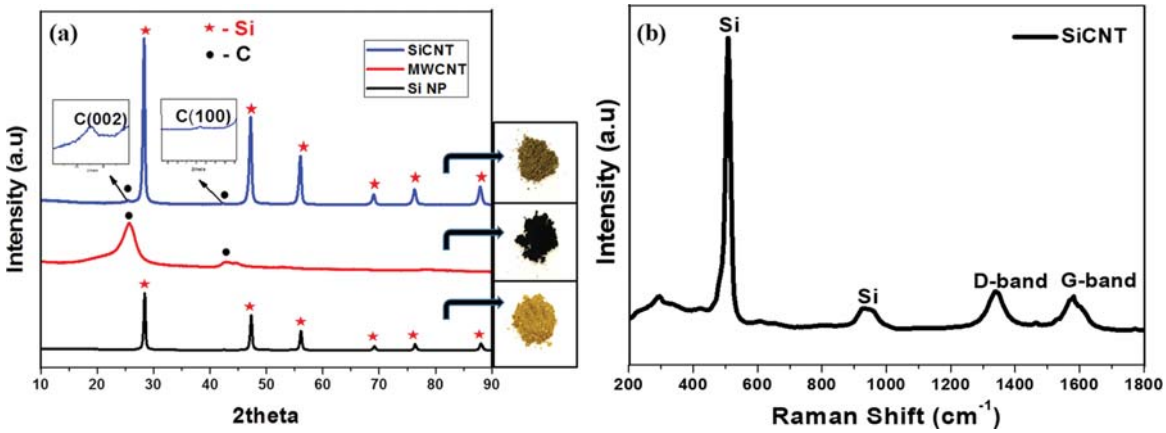

Fig. 2. (a) XRD patterns of Si nanoparticles, MWCNT, and SiCNT composite samples with their corresponding powder images; (b) Raman spectra of SiCNT composite material.

uum oven for 3 h at 200 °C. After drying, the electrode was punched (14 mm diameter). The calculated mass loading of the active material on the copper foil was ~1.2 mg cm^{-2} with an average thickness of 150 μm. All coin cells were fabricated in the argon-filled glove box. Metallic lithium was employed as the counter electrode, and a polypropylene film was used as a separator. 1 M $LiPF_6$ in ethylene carbonate, diethyl carbonate, and fluoroethylene carbonate with a v/v ratio of 5 : 70 : 25 was used as an electrolyte. The electrochemical charge/discharge characteristics were measured within the 1C rate (0.1C for the 1st cycle, and 0.2C for 2nd cycle). All cells were observed within the 0.01-2.0 V window versus Li/Li^+. To analyze the redox behavior of the electrode, cyclic voltammetry (CV) tests were carried out between 0.01 to 2.0 V at a 0.1 mV s^{-1} scan rate. The specific capacities of the working electrode were determined based on the mass of the loaded active material.

RESULTS AND DISCUSSION

In Fig. 2(a), the XRD patterns of the Si nanoparticles, MWCNT, and the as-prepared SiCNT are shown. In the XRD patterns of Si nanoparticles, the main diffraction peaks for cubic crystalline Si are observed at 2θ=28.4°, 47.4°, 56.2°, 69.2° and 79.5° (JCPDS#27-1402) corresponding to the (111), (220), (311), (400), and (331) lattice planes, respectively. The XRD spectrum of MWCNT shows typical (002) and (100) peaks of carbon (see the insets of Fig. 2(a); 2θ of 26° and 43°). In Fig. 2(a), the right-side inset shows the images of Si nanoparticles (pale yellow color) and MWCNT (black color) powders. The XRD peaks of the as-prepared SiCNT composite exhibit intense diffraction peaks of Si together with small peaks of carbon (25.6° and 42.6°); this implies the formation of a Si-carbon composite [40-42], which was also confirmed by the exposed blackish-yellow–colored powder in the corresponding right-side inset image. Fig. 2(b) represents the Raman spectra of the SiCNT composite; the active modes located at 510 cm^{-1} and 931 cm^{-1} bear a resemblance to crystalline Si. Moreover, the peaks at 1,340 cm^{-1} (D-band) and 1,585 cm^{-1} (G-band) indicate structural defects in the carbon due to sp^2 graphitic carbon, suggesting Si-carbon composite formation [43-45]. SEM, TEM, and TGA results of SiCNT

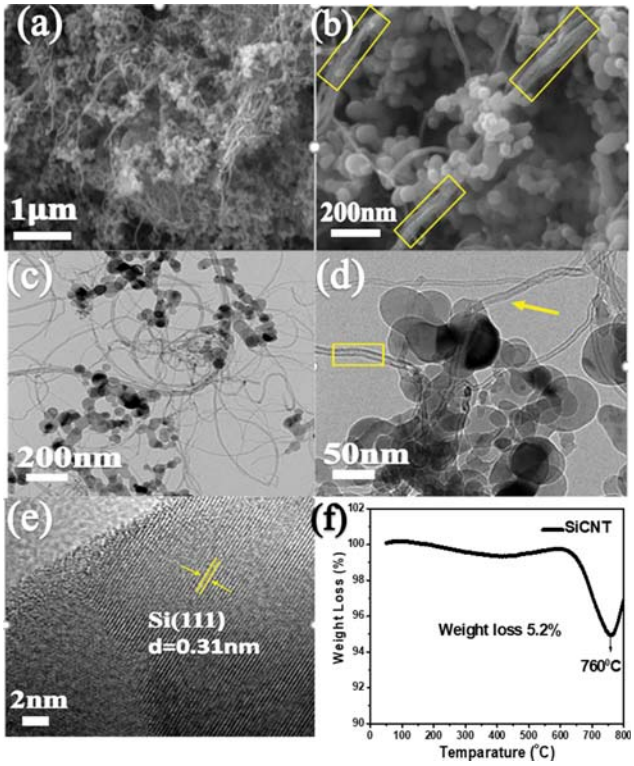

Fig. 3. SEM image of (a) SiCNT composite; (b) magnified view of a specified place in image (a) (the colored boxes indicate the CNTs with porous walls). The TEM image of (c) SiCNT composite; the colored arrows indicate the surface defected CNTs; (d) magnified TEM image of SiCNT. (e) HRTEM of a particular silicon nanoparticle. (f) TGA curve of SiCNT.

are shown in Fig. 3. As illustrated in Fig. 3(a), a low-magnification SEM image indicates aggregated silicon nanoparticles embedded into a dense MWCNT matrix. Fig. 3(b) shows the enlarged FESEM image of a specific portion of Fig. 3(a). The CNT porous wall defects with average pore size width lie in the range of 5-10 nm (marked with yellow-colored boxes). These porous walls were possibly intro-

duced during the annealing treatment. TEM images in Fig. 3(c) and 3(d) further reveal the microstructure of the SiCNT composite in which Si nanoparticles and CNTs are connected; the porous walls of the CNT are marked with yellow-colored boxes in Fig. 3(d). A high-resolution TEM image of specific Si nanoparticles reveals the crystalline characteristic, with a d-spacing of 0.31 nm matched to the (111) plane. Fig. 3(e) shows the TGA curve of the SiCNT composite. The TGA was performed in the air from room temperature to 800 °C at a heating rate of 10 °C per minute to determine the complete oxidation temperature of carbon and Si (Si to SiO_2). The carbon content in the composite was 5.2 wt% at 762 °C. Note that the amount of carbon content in the composite was lower than the actual weight of the added CNTs in the experiment. This could be attributed to the partial surface oxidation of the carbon nanotubes when annealing SiCNT at 400 °C.

Fig. 4(a) shows the first three cyclic voltammetry peaks of the SiCNT electrode. In the cathodic half, an extended broad peak exists at 0.6 V versus Li/Li^+, which takes into account the formation of a solid electrolyte interphase (SEI) on the surface of the electrode because of the reaction between the electrode material and electrolyte during its first discharge process. In the following cycles, this peak disappeared because of the formation of a stable SEI layer. Another notable cathodic peak at 0.18 V versus Li/Li^+ in the next cycles was attributed to the alloying process of Li_xSi. In the anodic half, the peaks at 0.35 V and 0.52 V represent the de-alloying process of Li_xSi to amorphous Si. The enhancement of these peaks in the subsequent cycles was due to the increased activation of the Si phase [40,46]. The electrochemical charge and discharge curves of the 1st, 2nd, 25th, and 50th cycles of the SiCNT and SKB electrodes cycled between the voltage limits of 0.01 V-2 V versus Li/Li^+ at 1C (1C is defined as 3.6 A g^{-1} concerning the mass of SiCNT, which is 80 wt% of the electrode) are displayed in Fig. 4(b) and Fig. 4(c), respectively. During the first discharge process, SiCNT and SKB electrodes exhibit a distinct plateau at around 1.0 V to 0.05 V, respectively. This can be attributed to the decomposition of the electrolyte, which leads to the formation of a SEI layer on the surface of the electrode material. However, this plateau disappears in the following cycles, which indicates the formation of a stable SEI layer. In the first charging process, the broad plateau at around 0.22 V to 0.52 V can be attributed to the de-alloying process of the Li_xSi phase, which was observed in both electrodes. When compared with the SKB electrode, the SiCNT electrode exhibits high initial discharge and charge capacities of about 4,541 and 3,802 mAh g^{-1}, respectively, with a 739 mAh g^{-1} irreversible capacity loss through the 83.7% initial Coulombic efficiency (ICE). On the other hand, the SKB electrode delivers 3,320 mAh g^{-1} and 2,572 mAh g^{-1} discharge and charge capacities with 748 mAh g^{-1} irreversible capacity loss (ICE is 77.4%). In Fig. 4(d), the cycling performance of the SiCNT and SKB electrodes at a 1C rate together with the CE values of SiCNT are shown. The ICE for SiCNT is superior to that of the SKB electrode. Moreover, it is greater than that of other well-fabricated Si/carbon reported composite materials [41,46-48]. The CE and discharge capacities of SiCNT and SKB electrodes for the second cycle are 91.5%, 3,792 mAh g^{-1}; and 76.1%, 2,292 mAh g^{-1}, respectively. However, the SKB electrode exhibits a decline in capacity up to the 35th cycle; capacity decreases from 500 to 254 mAh g^{-1}

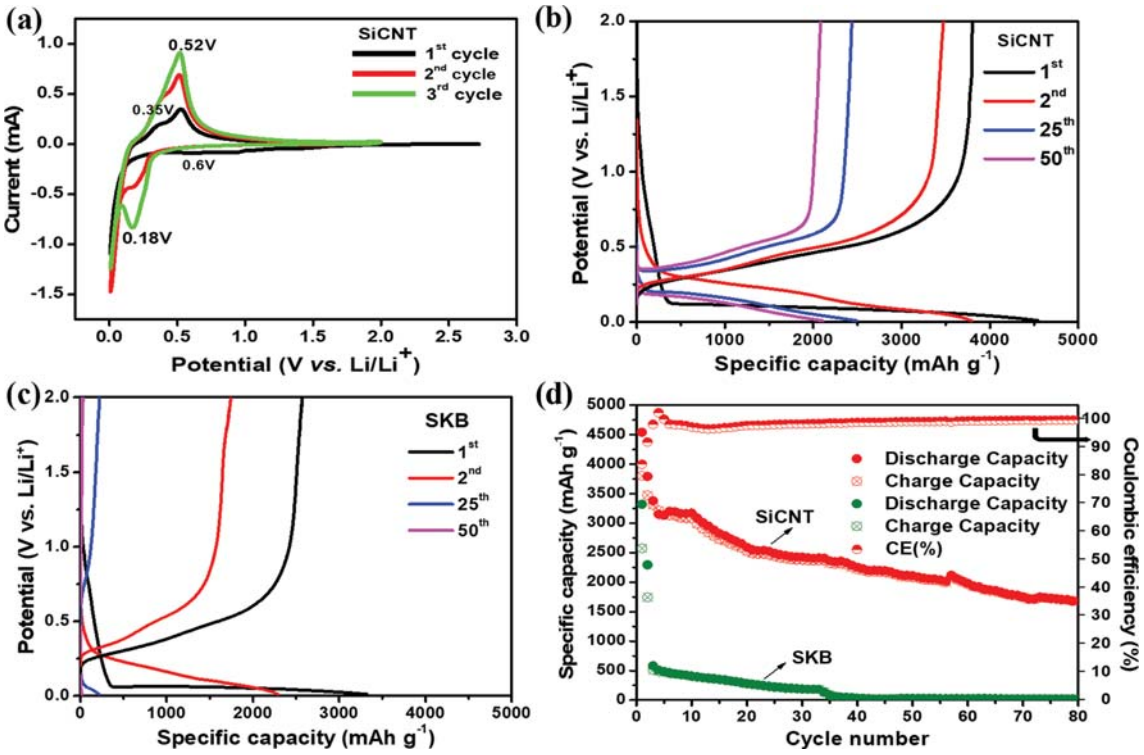

Fig. 4. (a) Cyclic voltammograms of the first 3 cycles of SiCNT from 0.01 V to 2 V at a scan rate of 0.1 mV s^{-1}; (b) and (c) charge and discharge voltage profiles of SiCNT and SKB electrodes for the 1st, 2nd, 25th, and 50th cycles tested between 0.01 V and 2 V at a rate of 1C, and (d) cycling behavior of both electrodes with a Coulombic efficiency of SiCNT composite at a rate of 1C.

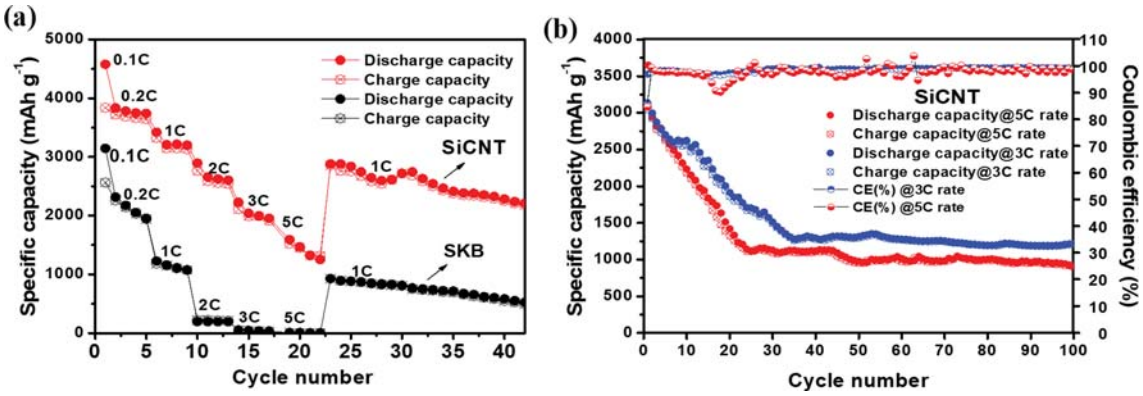

Fig. 5. (a) Rate capability of SiCNT and SKB electrodes at different current densities; (b) cycling behavior and Coulombic efficiency of SiCNT composite at 3C and 5C.

(fade rate of 7.15% loss/cycle for 35 cycles). Subsequently, a rapid capacity fade was observed with a discharge capacity close to double-digits (22 mAh g^{-1} after the 80th cycle). At the end of the 80th cycle, the SiCNT electrode shows a capacity of 1,685 mAh g^{-1}, with 99.5% of CE. About 65% of capacity retention is achieved by the SiCNT electrode from the 20th cycle to the 80th cycle. This significant improvement in the cycle stability of the SiCNT, when compared to the SKB electrode, can be attributed to the CNT matrix within the composite, which provides not only conductive support, but also excellent mechanical stability to the Si nanoparticles attached to the CNT walls. In addition, the porous walls of CNTs assist the enhanced electrochemical properties of the SiCNT composite. Fig. 5(a) shows the rate capability of the SiCNT and SKB electrodes at charge/discharge rates of 0.1C, 0.2C, 1C, 2C, 3C, and 5C. The SiCNT electrode exhibits reversible discharge capacities of 4,575, 3,832, 3,420, 2,893, 2,225 and 1,592 mAh g^{-1} at 0.1, 0.2, 1, 2, 3 and 5C current densities, respectively. Even at higher current rates of 2C, 3C, and 5C, the capacity remained more than 2,000, 1,500, and 1,000 mAh g^{-1}, respectively, which is almost three-fold higher than the capacity exhibited by commercial-grade graphite anodes. These capacity values surpass the reported Si-carbon-based hybrid electrodes with various morphologies [49-51]. The capacity was recovered to 2,878 mAh g^{-1} when the rate was reduced to 1C after being cycled at a 5C rate, which is higher than the initially obtained capacities at the 2C rate. As regards the SKB electrode, when the current rate was increased from 0.1C to 5C, the capacities were drastically decreased and almost reached zero at 5C. The poor cycling and rate performance can be attributed to the pulverization of Si nanoparticles during the crumbling of the electrode material. The formation of the Li-Si alloy during cycling induces significant volume expansion, which can lead to the creation of micro-cracks on the electrode surface, resulting in loss of contact with the current collector, and this consequently results in poor cycle retention. This result suggests that the combination of Si nanoparticles with CNTs greatly enhanced the cycling capability of the composite SiCNT by providing an electrically conductive network and facile strain relaxation afforded by CNTs. Further, the superior mechanical strength of CNTs can help anchor active Si nanoparticles and prevent aggregation during cycling. In Fig. 5(b), we cycled the SiCNT cells at higher rates of between 2 V and 0.01 V. Initially, at high current rates of 3C and 5C, the discharge capacity of SiCNTs exhibited high values of 3,276 mAh g^{-1} and 3,648 mAh g^{-1}, respectively; moreover, they remained at 968 mAh g^{-1} and 913 mAh g^{-1} at 3C and 5C, respectively, after 100 cycles. SiCNTs also exhibited good CEs of 86.2% at 3C and 84.6% at 5C for their initial cycles and ended at high efficiency of greater than 98%. After a total of 100 cycles, the cells showed capacity retention of 67% (versus the 25th cycle) at 3C and 80% (versus the 25th cycle) at 5C, respectively.

The TEM image of the electrode, which was cycled at 3C for 100 cycles, is shown in Fig. 6(a) and Fig. 6(b). The image indicates the amorphous phase and aggregated nanoparticles of Si firmly connected to the fragmented CNT segments (marked with colored arrows in Figs. 6(a), (b), and (c)) with the rugged SEI layer (spotted with black arrows in Fig. 6(b)). Though the electrode cycled such high current density, there was inconsequential structural damage and the SiCNTs exhibited good structural integrity. More importantly, some portion of the amorphous silicon was smeared into the irregular defected pores of CNTs (marked with yellow-colored arrows in Fig. 6(c)) and remained firmly connected to the conductive CNT walls during cycling, and thereby proved to be highly resistant to the volume changes associated with Si expansion. Therefore, the superior performance of the proposed electrode can be attributed to the increased Si volume and the mechanical integrity of the Si/CNT/SEI layer. Fig. 6(d) shows a schematic diagram of the Si/CNT vs. Li/Li^+ half-cell, where porous CNT provides a conductive network for Li-ion reactions with Si particles and CNT walls; after 100 cycles, image Fig. 6(c) demonstrates structural stability. To assess the reproducibility of the proposed system, TEM images of the composite R-SiCNT were taken (Fig. 7(a) and (b)). From the images the porous MWCNTs and composite formation indicated with yellow arrows can be observed, and it is clear that these structures are similar to that of Si/porous MWCNT structures depicted in Fig. 3(c) and (d), indicating the possibility of reproducibility of the system. The final yield of this composite was 92.7%. When compared with the SiCNT sample, the error in reproducibility was 0.54%, which shows our method is reproducible with repeated structures. All these attributes of the SiCNT electrode render it an easily reproducible and superior anode electrode material for LIBs. Moreover, the SiCNT nanocomposite obtained using

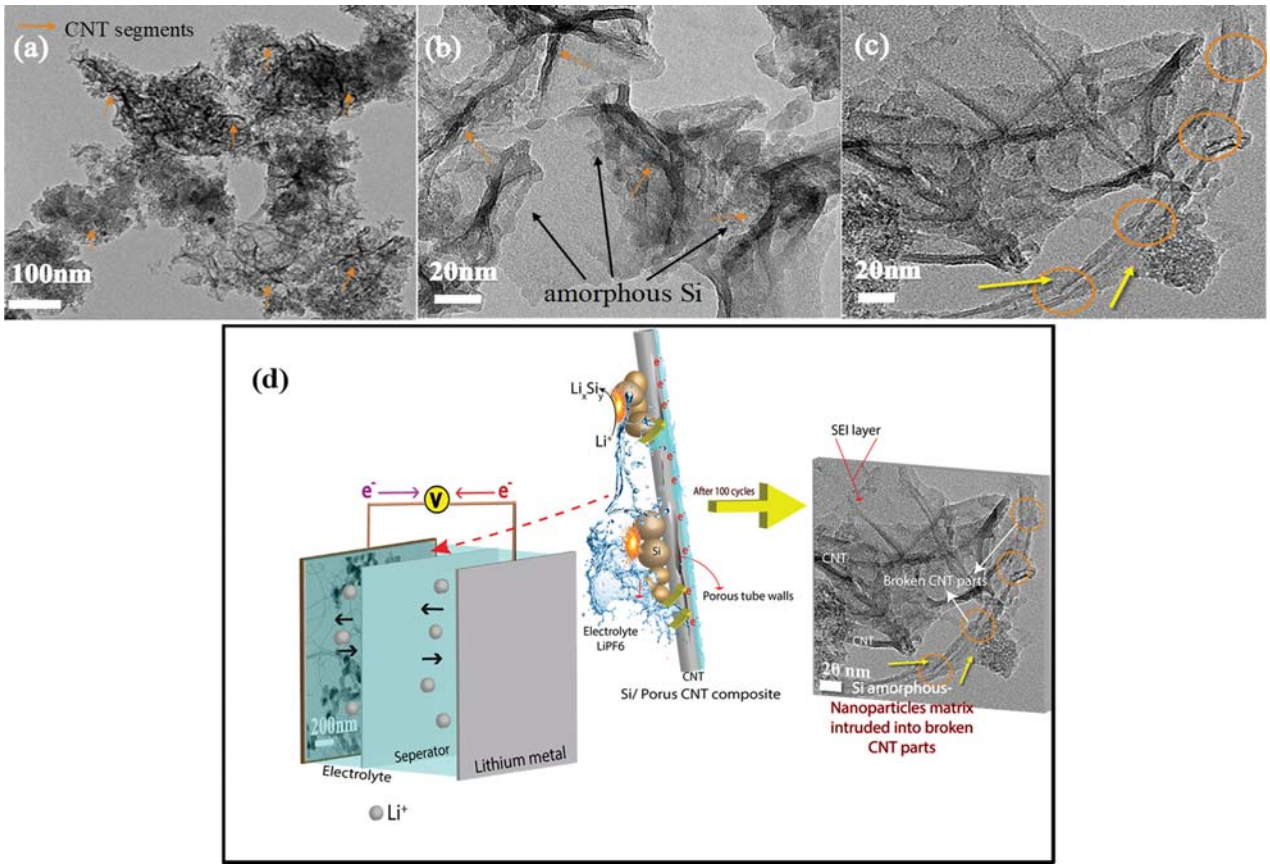

Fig. 6. (a) TEM image of SiCNT composite after 100 cycles at 3C; the small orange-colored arrows indicate CNT segments; (b) magnified view of (a); (c) amorphous silicon smeared into CNT segments (marked with yellow arrows) integrated network. (d) schematic diagram of Si/porous CNT reactions with the electrolyte and after cycling depicts image 6(c) composed of portions of CNT with amorphous Si.

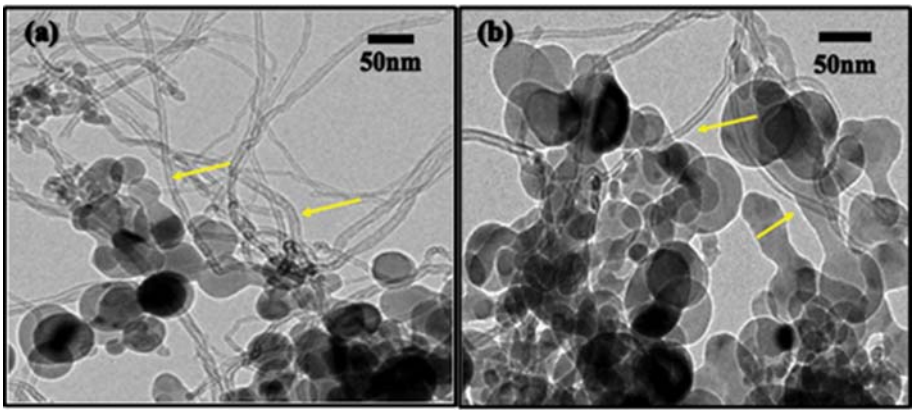

Fig. 7. (a) and (b) TEM images of R-SiCNT sample (formation of defected CNTs and SiCNT composite shown with yellow arrows).

this method exhibits competitive and better cycle performance than that reported on a variety of Si/CNT nanocomposites (Table 1). Our proposed synthesis method, without the use of any sophisticated equipment and with low-temperature annealing, simple experimental conditions, and excellent reproducibility, is suitable for producing efficient carbon composite materials at a low cost for a wide variety of energy storage applications.

CONCLUSION

A porous SiCNT hybrid nanocomposite comprising silicon nanoparticles was successfully integrated with a porous MWCNTs matrix. The hybrid nanocomposite was synthesized through a simple two-step process involving mini-milling followed by low-temperature annealing. When used as a Li-ion battery anode, the prepared

Table 1. Comparison of electrochemical performance of different Si/CNT-based nanocomposites with our results

Composite materials	Current density (mA g^{-1}) or 1C=~3.6 Ag^{-1}	Reversible specific capacity (mAh g^{-1})	References
Multi-walled carbon nanotube-embedded silicon nanoparticle films	840, 100 cycles	1,510	39
Nanostructured hybrid silicon/carbon nanotubes heterostructures	2.5C, 5 cycles	~1,000	41
Scribble multi-walled carbon nanotubes-silicon nanocomposite	300, 50 cycles and 2,000, 5 cycles	2,250 and 1,550	47
Light-weight free-standing carbon nanotubes-silicon films	360, 5 cycles and 1,200, 50 cycles.	~2,400 and ~1,900	51
Si-MWNT nanocomposite	500, 10 cycles	~800	52
Single-walled carbon nanotubes/silicon composites	50, 50 cycles	~1,400	53
Silicon/porous multi-walled carbon nanotubes composite	1C, 80 cycles and 5C, 100 cycles	2,000 and 1,100	This work

composite electrode exhibited high reversible capacity, excellent cycle stability, and rate capability. The notable improvements in electrochemical properties can be attributed to the collective outcome of both silicon nanoparticles and porous CNTs. The CNTs with defective porous walls appearing in the composite provide a flexible conductive matrix that can endure severe volume changes in the Si nanoparticles which are brought upon by lithium-ion reactions and prevent electrode pulverization. Moreover, the excellent cycling performance of the proposed composite, even at high current densities of 3C and 5C, can be attributed to the robust adherence of amorphous silicon onto the flexible porous CNT segments. This excellent performance makes the fabricated composite a promising anode material for lithium-ion batteries. These results, together with the simplicity of the proposed approach, provide an inexpensive and facile synthesis strategy for the development of efficient electrode materials for energy storage applications.

ACKNOWLEDGEMENTS

This research was partly funded by grants (NRF-2015R1D1A1A01059983 and NRF-2018R1D1A1B07044026) from the Basic Science Research Program through the National Research Foundation of Korea (NRF) which is funded by the Ministry of Education. We thank them for their financial support.

REFERENCES

1. B. Scrosati, *Nature*, **373**, 557 (1995).
2. J. M. Tarascon and M. Armand, *Nature*, **414**, 359 (2001).
3. M. N. Obrovac and L. Christensen, *Electrochem. Solid-State Lett.*, **7**, A93 (2004).
4. M. Armand and J. M. Tarascon, *Nature*, **451**, 7179 (2008).
5. N. Nitta, F. Wu, J. T. Lee and G. Yushin, *Mater Today*, **18**, 252 (2015).
6. Y. P. Wu, E. Rahm and R. Holze, *J. Power Sources*, **114**, 2 (2003).
7. D. H. Liu, H. Y. Lu, X. L. Wu, J. Wang, X. Yan, J. P. Zhang, H. Geng, Y. Zhang and Q. Yan, *Nanoscale Horiz.*, **1**, 6 (2016).
8. H. Li, X. Huang, L. Chen, Z. Wu and Y. Liang, *Electrochem. Solid-State Lett.*, **2**, 11 (1999).
9. H. Ma, F. Cheng, J. Chen, J. Zhao, C. Li, Z. Tao and J. Liang, *Adv. Mater.*, **19**, 22 (2007).
10. J. R. Szczech and S. Jin, *Energy Environ. Sci.*, **4**, 1 (2011).
11. T. Song, J. Xia, J. H. Lee, D. H. Lee, M. S. Kwon, J. M. Choi, J. Wu, S. K. Doo, H. Chang, W. I. Park, D. S. Zang, H. Kim, Y. Huang, K. C. Hwang, J. A. Rogers and U. Paik, *Nano Lett.*, **10**, 5 (2010).
12. J. Xiao, W. Xu, D. Wang, D. Choi, W. Wang, X. Li, G. L. Graff, J. Liu and J. G. Zhanget, *J. Electrochem. Soc.*, **157**, 10 (2010).
13. J. W. Wang, Y. He, F. Fan, X. H. Liu, S. Xia, Y. Liu, C. T. Harris, H. Li, J. Y. Huang, S. X. Mao and T. Zhu, *Nano Lett.*, **13**, 2 (2013).
14. Y. Yu, L. Gu, C. Zhu, S. Tsukimoto, P. A. VanAken and J. Maier, *Adv. Mater.*, **22**, 20 (2010).
15. Y. Zhang, Y. Zhu, L. Fu, J. Meng, N. Yu, J. Wang and Y. Wu, *Chin. J. Chem.*, **35**, 1 (2017).
16. Z. S. Wen, J. Yang, B. F. Wang, K. Wang and Y. Liu, *Electrochem. Commun.*, **5**, 2 (2003).
17. L. Fagiolari and F. Bella, *Energy Environ. Sci.*, **12**, 3437 (2019).
18. L. L. Perreault, F. Colò, G. Meligrana, K. Kim, S. Fiorilli, F. Bella, J. R. Nair, C. V. Brovarone, J. Florek, F. Kleitz and C. Gerbaldi, *Adv. Energy Mater.*, **8**, 1802438 (2018).
19. H. Sun, J. Zhu, D. Baumann, L. Peng, Y. Xu, I. Shakir, Y. Huang and X. Duan, *Nat. Rev. Mat.*, **4**, 45 (2019).
20. J. H. Jeong, D. W. Jung, B. S. Kong, C. M. Shin and E. S. Oh, *Korean J. Chem. Eng.*, **28**, 2202 (2011).
21. N. Venugopal, W. S. Kim and T. Yu, *Korean J. Chem. Eng.*, **33**, 1500 (2016).
22. O. M. Vovk, B. K. Na, B. W. Cho and J. K. Lee, *Korean J. Chem. Eng.*, **26**, 1034 (2009).
23. N. Venugopal and W. S. Kim, *Korean J. Chem. Eng.*, **32**, 1918 (2015).
24. A. Pedico, A. Lamberti, A. Gigot, M. Fontana, F. Bella, P. Rivolo, M. Cocuzza and C. F. Pirri, *ACS Appl. Energy Mater.*, **1**, 4440 (2018).
25. J. Liu, D. Li, Y. Wang, S. Zhang, Z. Kang, H. Xie and L. Sun, *J. Energy Chem.*, **47**, 66 (2020).
26. Q. Luo, H. Ma, Q. Hou, Y. Li, J. Ren, X. Dai, Z. Yao, Y. Zhou, L. Xiang, H. Du, H. He, N. Wang, K. Jiang, H. Lin, H. Zhang and Z. Guo, *Adv. Funct. Mater.*, **28**, 1706777 (2018).

27. H. J. Shih, J. Y. Chang, C. S. Cho and C. C. Li, *Carbon*, **159**, 401 (2020).
28. F. Bella, D. Pugliese, L. Zolin and C. Gerbaldi, *Electrochim. Acta*, **237**, 87 (2017).
29. L. Zolin, J. R. Nair, D. Beneventi, F. Bella, M. Destro, P. Jagdale, I. Cannavaro, A. Tagliaferro, D. Chaussy, F. Geobaldo and C. Gerbaldi, *Carbon*, **107**, 811 (2016).
30. Y. Zhang, Y. Zhu, L. Fu, J. Meng, N. Yu, J. Wang and Y. Wu, *Chin. J. Chem.*, **35**, 1 (2017).
31. Z. S. Wen, J. Yang, B. F. Wang, K. Wang and Y. Liu, *Electrochem. Commun.*, **5**, 2 (2003).
32. Q. Si, M. Kawakubo, M. Matsui, T. Horiba, O. Yamamoto, Y. Takeda, N. Seki and N. Imanishi, *J. Power Sources*, **248**, 1275 (2014).
33. Y. M. Chiang, *Science*, **330**, 6010 (2010).
34. K. Saeed and I. Khan, *Carbon Lett.*, **14**, 3 (2013).
35. S. Iijima, *Nature*, **354**, 56 (1991).
36. K. Wang, S. Luo, Y. Wu, X. He, F. Zhao, J. Wang, K. Jiang and S. Fan, *Adv. Funct. Mater.*, **23**, 7 (2013).
37. A. Gohier, B. Laïk, K. H. Kim, J. L. Maurice, J. P. P. Ramos, C. S. Cojocaru and P. T. Van, *Adv. Mater.*, **24**, 19 (2012).
38. W. Wang, R. Epur and P. N. Kumta, *Electrochem. Commun.*, **13**, 5 (2011).
39. K. S. Park, K. M. Min, S. D. Seo, G. H. Lee, H. W. Shim and D. W. Kim, *Mater. Res. Bull.*, **48**, 4 (2013).
40. G. Hatipoglu, M. Alaf and H. Akbulut, *J. Mater. Sci.: Mater. Electron.*, **3**, 2067 (2019).
41. W. Wang and P. N. Kumta, *ACS Nano.*, **4**, 4 (2010).
42. L. Ji and X. Zhang, *Carbon*, **47**, 14 (2009).
43. A. K. Arora, M. Rajalakshmi, T. R. Ravindran and V. Sivasubramanian, *J. Raman Spectrosc.*, **38**, 6 (2007).
44. J. Cebik, J. K. McDonough, F. Peerally, R. Medrano, I. Neitzel, Y. Gogotsi and S. Osswald, *Nanotechnology*, **24**, 20 (2013).
45. H. F. Arani, A. R. Mirhabibi, S. Collins, R. Daroughegi, A. K. Soltani, R. Aghizadeh, N. R. Noori, R. Aghababazadeh and A. Westwood, *RSC Adv.*, **7**, 9 (2017).
46. X. Shen, D. Mu, S. Chen, B. Xu, B. Wu and F. Wu, *J. Alloy Compd.*, **552**, 60 (2013).
47. R. Epur, M. Ramanathan, M. K. Datta, D. H. Hong, P. H. Jampani, B. Gattu and P. N. Kumt, *Nanoscale*, **7**, 8 (2015).
48. N. Arunakumari, N. Venugopal and K. Y. Sohn, *Sci. Adv. Mater.*, **12**, 337 (2020).
49. L. F. Cui, Y. Yang, C. M. Hsu and Y. Cui, *Nano Lett.*, **9**, 9 (2009).
50. X. Yang, Z. Wen, X. Xu, B. Lin and Z. Lin, *J. Electrochem. Soc.*, **153**, 7 (2006).
51. L. F. Cui, L. Hu, J. W. Choi and Y. Cui, *ACS Nano.*, **4**, 7 (2007).
52. P. Gao, Y. Nuli, Y. S. He, J. Wang, A. I. Minett, J. Yang and J. Chen, *Chem. Commun.*, **46**, 48 (2010).
53. J. Y. Eom and H. S. Kwon, *ACS Appl. Mater. Interfaces*, **3**, 4 (2011).